CHEMISTRY OF MATERIALS

pubs.acs.org/cm

Article

Expanding the Family of Magnetic Vacancy-Ordered Halide Double Perovskites

Kurt P. Lindquist,* Teresa Lee, Xianghan Xu, and Robert J. Cava*

Cite This: *Chem. Mater.* 2024, 36, 7610−7618

Read Online

ACCESS | Metrics & More | Article Recommendations | Supporting Information

ABSTRACT: Vacancy-ordered halide double perovskites, with the general formula $A_2^{I}B^{IV}X_6$, can accommodate a wide variety of tetravalent B-site cations. However, few examples containing trivalent B-site cations exist, limiting the variety of magnetic cations that can comprise this structure type. Here, we incorporate divalent A-site cations to form the vacancy-ordered double perovskites $A^{I}A^{II}B^{III}Cl_6$ (A^{I} = Na, K, Rb, Cs; A^{II} = Sr, Ba; B^{III} = Ti, V, Cr, Ir) and $Ba_{1.5}B^{III}Cl_6$ (B^{III} = V, Cr). By tuning the radius of the A-site through cation substitution, we form four structure-types with these formulas, including a K_2PtCl_6-type structure, a low-temperature K_2SnCl_6-type structure, a novel derivative with ordered A^{1+}/A^{2+} cations, and a second novel derivative with ordered A-site vacancies. This structural diversity, which includes 22 unique compositions, allows us to study the effect of structure and composition on the magnetic properties of these solids, which show antiferromagnetic coupling of weak-to-moderate strength and signatures of frustrated long-range ordering. Furthermore, our studies of temperature-dependent magnetism and heat capacity reveal that the magnetic coupling strength decreases with octahedral tilting, consistent with expectations; in contrast, the coupling strength counterintuitively increases from B^{III} = Ti to Cr to V, which we speculate may be a result of competing antiferromagnetic and ferromagnetic interactions. By substituting divalent A-site cations into vacancy-ordered halide double perovskites, we further expand the already rich phase space of these structures to include magnetic trivalent transition metals and deepen our understanding of structure−magnetism relationships in metal halides.

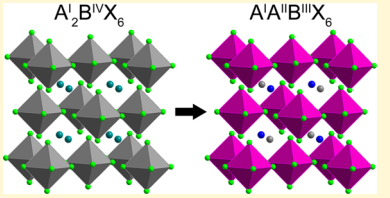

INTRODUCTION

As metal−halide perovskites have come to research prominence for their optoelectronic properties, a large variety of new halide-perovskite compositions and structural derivatives are regularly being discovered and characterized. While the focus has largely been on the main-group-element-based compositions due to their high performance in optoelectronic devices,[1,2] the relative dearth of transition-metal-based halide perovskites offers a tantalizing opportunity to explore new compositions with magnetic cations.[3] Furthermore, drawing structure−property relationships in magnetic metal halides will facilitate a deeper understanding of the interactions between composition, geometry, and magnetism in metal halides, paving the way toward their use in, for example, spintronics[4] and data storage.[5]

The vacancy-ordered halide double perovskites (VDPs), having the general formula $A_2^{I}B^{IV}X_6$ where A is a monovalent cation, B is tetravalent metal, and X is a halide, can accommodate a wide swath of the periodic table into their B-site, including several magnetic B-site cations.[6] Because the metal-halide octahedra are disconnected in this structure type, they are of particular interest to study the behavior of magnetic and electronic interactions across vacant space. In these VDPs, the primary magnetic interactions are supersuperexchange, wherein the magnetic centers communicate through two halide centers via M−X···X−M.[7] The distance between adjacent B-site cations and the tilt angles of the metal-halide octahedra can be adjusted by changing the composition, yielding an effective method of studying the effects of these structural factors on magnetic supersuperexchange interactions. Thus, magnetic VDPs offer a readily tunable platform to study structure−magnetism relationships.

Despite their compositional diversity, the charge of the B-site cation in VDPs is generally limited to 4+. One strategy to incorporate cations with different charges than the prototypical structure is to split one occupant of the structure into two distinct cations, for example by splitting the B-site in $Cs_3^{I}Sb_2^{III}Cl_9$ to form $Cs_4^{I}Cu^{II}Sb_2^{III}Cl_{12}$ or $Cs_3^{I}Bi_2^{III}Cl_9$ to form $Cs_4^{I}Cd^{II}Bi_2^{III}Cl_{12}$.[8,9] In VDPs, this strategy can be used to incorporate 3+ B-site cations by splitting the A-site into 1+ and 2+ cations, yielding the formula $A^{I}A^{II}B^{III}X_6$. This strategy greatly expands the available B-site cations available to these compositions by accommodating a 3+ charge but has so far been limited to a handful of noncubic fluoride-based compositions, such as $Li^{I}Ba^{II}Cr^{III}F_6$,[10] $Li^{I}Mn^{II}Fe^{III}F_6$,[11] $Li^{I}Sr^{II}Al^{III}F_6$,[12] and $Na^{I}Sr^{II}Fe^{III}F_6$.[13] Because chloride-based compositions are typically easier to synthesize and have stronger interoctahedral electronic interactions than their

Received: July 6, 2024
Revised: July 9, 2024
Accepted: July 11, 2024
Published: July 17, 2024

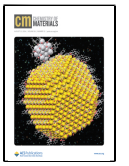

Table 1. Currently Reported Compositions Organized by Structure Type, Including Unit-cell Volumes and Radius Ratios from X-ray Diffraction Data at 300 K[a,23]

structure type	composition	average A-site Shannon radius	norm. unit-cell volume (Å^3)	radius ratio
$Ba_{1.5}CrCl_6$	$Ba_{1.5}VCl_6$[b]	1.21	913.3(5)	0.69 (0.61−0.81)
	$Ba_{1.5}CrCl_6$	1.21	896.43(13)	0.70 (0.61−0.82)
$NaBaCrCl_6$	$NaBaTiCl_6$	1.50	930.04(3)	0.76 (0.72−0.82)
	$NaBaVCl_6$[b]	1.50	902.00(14)	0.81 (0.74−1.02)
	$NaBaCrCl_6$	1.50	889.45(3)	0.77 (0.71−0.85)
LT K_2SnCl_6	$NaSrTiCl_6$[b]	1.42	906.56(10)	0.71 (0.66−0.76)
	$NaSrVCl_6$[b]	1.42	876.14(10)	0.73 (0.65−0.83)
	$NaSrCrCl_6$	1.42	863.74(4)	0.73 (0.67−0.79)
	$KSrTiCl_6$[b]	1.54	948.0(2)	0.80 (0.74−0.88)
	$KSrVCl_6$[b]	1.54	924.52(14)	0.80 (0.71−0.87)
	$KSrCrCl_6$	1.54	907.9(3)	0.80 (0.72−0.84)
	$RbSrVCl_6$[b]	1.58	948.0(4)	0.87 (0.77−1.11)
K_2PtCl_6	$RbSrCrCl_6$	1.58	928.37(9)	0.87
	$KBaTiCl_6$[c]	1.63	965.9(2)	0.92
	$KBaVCl_6$	1.63	926.92(6)	0.93
	$KBaCrCl_6$	1.63	907.12(14)	0.93
	$KBaIrCl_6$	1.63	904.65(6)	0.95
	$RbBaTiCl_6$	1.67	968.45(9)	0.93
	$RbBaVCl_6$	1.67	942.14(6)	0.93
	$RbBaCrCl_6$	1.67	924.89(6)	0.94
	$CsBaTiCl_6$	1.75	1005.29(12)	0.93
	$CsBaVCl_6$	1.75	982.08(6)	0.93
	$CsBaCrCl_6$	1.75	965.2(2)	0.94

[a]For ease of comparison, the unit-cell volume for the $Ba_{1.5}CrCl_6$ structure type was normalized by dividing by eight to account for the doubled lattice parameters with respect to the K_2PtCl_6-type structure, while the unit-cell volumes for the low-temperature (LT) K_2SnCl_6 structure type were doubled to account for the reduction in symmetry. The radius ratios shown for the $Ba_{1.5}CrCl_6$, $NaBaCrCl_6$, and LT K_2SnCl_6 structure types are calculated from the average of the nearest-neighbor Cl−Cl distances (within 4 Å), while the ranges in parentheses were calculated using the shortest and longest Cl−Cl distances (within 4 Å). The ionic radii were taken from ref 23. [b]Values obtained from Rietveld refinement of PXRD data. All other values were obtained from SCXRD data. [c]$KBaTiCl_6$ has an unresolved superstructure; the values shown are for the K_2PtCl_6-type structure solution and are taken as estimates.

fluoride congeners, expanding the family of magnetic Cl-based VDPs would constitute a significant advance in the study of magnetic halide perovskites. Here, we combine 1+ and 2+ A-site cations to incorporate 3+ B-site cations into Cl-based VDPs, forming 22 new magnetic VDP compositions with four distinct structure types, two of which are previously unreported structures with no known analogs and exhibit A-site ordering, a phenomenon rarely observed in halide perovskites. We explore structure−property relationships, finding that these materials exhibit antiferromagnetic interactions, with possible competing ferromagnetic coupling, that vary with both the identity of the B-site cation and the degree of octahedral tilting. Furthermore, while short-range magnetic ordering is observed at temperatures commensurate with the strength of magnetic interactions, long-range magnetic ordering appears to be suppressed, which we ascribe to geometric frustration from the face-centered-cubic arrangement of the magnetic cations in these VDPs.

EXPERIMENTAL SECTION

Synthesis and Characterization. Due to the hygroscopicity of metal-halide salts, all manipulations of powders and crystals were performed in a N_2-filled glovebox, unless otherwise noted. All chemicals were dried overnight in a vacuum oven at 160 °C prior to being brought into the glovebox for use. The agate mortar and pestle used for grinding and the fused-silica tubes were baked in an oven at 120 °C for 45 min prior to bringing into the glovebox to remove adsorbed water.

Crystals and powders of $A^IA^{II}B^{III}Cl_6$ (A^I = Na, K, Rb, Cs; A^{II} = Sr, Ba; B^{III} = Ti, V, Cr, Ir) and $Ba_{1.5}B^{III}Cl_6$ (B^{III} = V, Cr) (see Table 1 for a list of the compositions) were synthesized by solid-state reactions in sealed fused-silica ampules. Stoichiometric amounts of $BaCl_2$ (Alfa Aesar, 99+%), $SrCl_2$ (Sigma-Aldrich, 99.99%), NaCl (Alfa Aesar, 99.998%), KCl (Sigma, 99.999%), RbCl (Alfa Aesar, 99.8%), CsCl (Alfa Aesar, 99.9%), $TiCl_3$ (Aldrich, ReagentPlus), VCl_3 (Beantown Chemical, 99%), $CrCl_3$ (Thermo Scientific, 99.9%), and/or $IrCl_3$ (Alfa Aesar, Ir ≥63.9%) as appropriate to the composition were ground using a mortar and pestle, with a typical total mass of 100 mg. A small excess (5−10 mol %) of $BaCl_2$ or $SrCl_2$ was used for most compositions to obtain powders free of magnetic BCl_3 impurities. The ground reagents were loaded into fused-silica tubes, fitted to a sealed vacuum fitting, brought out of the glovebox, and immediately fitted into a steel vacuum manifold for three cycles of evacuation followed by backfilling with Ar. The tubes were then flame-sealed under rough vacuum (~10^{-3} Torr). The ampules were placed into a box furnace and heated overnight with a heating and cooling rate of 180 °C·h^{-1}. Powders were synthesized using temperatures of 450 °C ($NaBaTiCl_6$, $KSrTiCl_6$, $KBaTiCl_6$, $CsBaTiCl_6$), 500 °C ($RbBaTiCl_6$), 550 °C ($NaSrVCl_6$), 600 °C ($NaBaVCl_6$, $RbSrVCl_6$, $KSrVCl_6$), 650 °C ($Ba_{1.5}CrCl_6$, $NaBaCrCl_6$, $NaSrCrCl_6$, $RbSrCrCl_6$, $KBaVCl_6$, $KBaCrCl_6$, $KBaIrCl_6$, $RbBaVCl_6$, $RbBaCrCl_6$, $CsBaVCl_6$, $CsBaCrCl_6$), 675 °C ($KSrCrCl_6$), and 700 °C ($Ba_{1.5}VCl_6$), while crystals suitable for single-crystal X-ray diffraction (SCXRD) were synthesized using temperatures of 650 °C ($NaBaTiCl_6$, $NaSrCrCl_6$, $RbSrCrCl_6$, $KBaTiCl_6$), 700 °C ($Ba_{1.5}CrCl_6$, $NaBaCrCl_6$, $KBaVCl_6$, $KBaCrCl_6$, $RbBaVCl_6$, $RbBaCrCl_6$, $CsBaVCl_6$), 750 °C ($KBaIrCl_6$, $CsBaCrCl_6$), and 800 °C ($KSrCrCl_6$, $RbBaTiCl_6$, $CsBaTiCl_6$). The current synthetic conditions did not provide crystals of sufficient quality for single-crystal X-ray diffraction for $Ba_{1.5}VCl_6$, $NaBaVCl_6$, $RbSrVCl_6$, $NaSrTiCl_6$, $NaSrVCl_6$, $KSrTiCl_6$, and $KSrVCl_6$. The materials were

https://doi.org/10.1021/acs.chemmater.4c01880
Chem. Mater. 2024, 36, 7610−7618

found to be highly sensitive to water content, for instance forming green CrOCl as a side product for Cr-based compositions if the sample was exposed to atmosphere or residual water was present in the fused-silica tubes prior to sealing.

Powder X-ray diffraction (PXRD) was carried out at room temperature inside a N_2-filled glovebox using a Rigaku Miniflex II diffractometer with a Cu anode and fixed divergence slits with a Ni filter. The instrument was operated in a Bragg–Brentano geometry with a step size of 0.02° (2θ). Powder X-ray diffraction on $Ba_{1.5}CrCl_6$ was carried out using a Bruker D8 Advance Eco diffractometer with a Cu anode, fixed divergence slits with a Ni filter, and a LYNXEYE detector. The instrument was operated in a Bragg–Brentano geometry with a step size of 0.01° (2θ). A bubble puck was used to protect the sample from the atmosphere. The high air sensitivity precluded the use of the Bruker instrument for many of the currently reported compositions; therefore, the Rigaku instrument was used for consistency, except where the greater resolution of the Bruker instrument was needed to resolve the peak splitting in $Ba_{1.5}CrCl_6$. Rietveld and Pawley refinement was carried out using the General Structure and Analysis System (GSAS II) software package.[14,15] The instrument parameters were determined from Si standards. The parameters refined were: scale factor, sample displacement, lattice parameters, atomic positions, size, and phase fraction of impurity(s), when applicable. The atomic positions were not refined for $Ba_{1.5}VCl_6$ and $Ba_{1.5}CrCl_6$ because the high number of unique atoms yielded unstable and unreliable fits; therefore, the atomic positions were fixed as those derived from single-crystal X-ray diffraction of $Ba_{1.5}CrCl_6$. For $Ba_{1.5}VCl_6$ and $Ba_{1.5}CrCl_6$, the lattice parameters were first determined using Pawley refinement, which were then imported and fixed for Rietveld refinement. Single crystal X-ray diffraction was carried out using a Bruker D8 Quest Eco diffractometer equipped with a Photon III CPAD detector and monochromated Mo Kα radiation. Crystals were coated with Cargille Type NVH immersion oil, mounted on a Kapton loop, and transferred to the diffractometer. Frames were collected using ω and ψ scans. An Oxford Cryostream was used to maintain an ambient of N_2 around the crystal and a temperature of 300 K. Unit-cell parameters were refined against all data. The crystals did not show significant decay during data collection. Frames were integrated and corrected for Lorentz and polarization effects using SAINT 8.40b and were corrected for absorption effects using SADABS V2016/2.[16] Space-group assignments were based upon systematic absences, *E*-statistics, agreement factors for equivalent reflections, and successful refinement of the structure. The structures were solved by direct methods, expanded through successive difference Fourier maps using SHELXT, and refined against all data using the SHELXL-2018[17] software package as implemented in Olex2.[17−20] Weighted *R* factors, R_w, and all goodness-of-fit indicators are based on F^2. Thermal displacement parameters for all atoms were refined anisotropically. The tabulated crystallographic data are presented in Tables S1–S47.

Magnetization measurements were performed using a Quantum Design Physical Properties Measurement System (PPMS) Dynacool. Plastic sample holders were used to immobilize 10–25 mg of powdered samples for measurement. Temperature-dependent direct-current (DC) magnetization (M) measurements were carried out from 1.8 to 300 K in applied magnetic fields ($\mu_0 H$) of 0.1 T, while magnetic-field-dependent measurements were carried out in applied magnetic fields from 0 to 9 T at a temperature of 1.8 K. The magnetization data were transformed to magnetic susceptibility, χ, by $M \cdot (\mu_0 H)^{-1}$, and inverted and plotted against temperature to fit to the Curie–Weiss law

$$\chi = \chi_0 + \frac{C}{T - \Theta_{CW}} \tag{1}$$

where C is the Curie constant, Θ_{CW} is the Curie–Weiss temperature, and χ_0 is the temperature-independent contribution to susceptibility. For $A^IA^{II}B^{III}Cl_6$ (B^{III} = Ti, V) and $Ba_{1.5}VCl_6$, the susceptibility was first fit directly (without inversion) to extract χ_0 before using the corrected inverse susceptibility plots for Curie–Weiss fitting. The fits were made over the temperature range 50–100 K for compositions with Ti and over 100–175 K for compositions with V and Cr to avoid both the low-temperature regime, where Curie–Weiss behavior may not hold, and the high-temperature regime, where the susceptibilities of $A^IA^{II}B^{III}Cl_6$ (B^{III} = Ti, V) and $Ba_{1.5}VCl_6$ were significantly influenced by χ_0. The effective magnetic moment was determined by

$$\mu_{eff} = \sqrt{\frac{3k_B}{N_A \mu_B^2} C} \tag{2}$$

where μ_{eff} is the effective magnetic moment in units of Bohr magnetons (μ_B).

Heat-capacity measurements were carried out using the same PPMS equipped with a ^{3}He refrigerator. Pressed pellets of neat powder were affixed to the sapphire measurement platform using Apiezon-N grease. The contribution of the sample holder with grease was subtracted after measuring it separately. Heat capacity was normalized to the sample mass. The nonmagnetic contribution to the heat capacity, i.e., the phonon contribution, was estimated by a two-component Debye equation

$$C_{phonon} = 9R \sum_{n=1}^{2} C_n \left(\frac{T}{\Theta_{Dn}}\right)^3 \int_0^{\Theta_{Dn}/T} \frac{x^4 e^x}{(e^x - 1)^2} dx \tag{3}$$

The fitting was performed in the temperature range 40–90 K, giving Θ_{D1} = 148.6 K and Θ_{D2} = 411.6 K for $KBaVCl_6$, and Θ_{D1} = 152.5 K and Θ_{D2} = 462.2 K for $KBaCrCl_6$. The sum of C_1 and C_2 of each compound was fixed at 9, corresponding to the total number of atoms in the chemical formula.

Ultraviolet–visible diffuse reflectance spectra (UV–vis) were collected using an Agilent Cary 5000 spectrophotometer equipped with an integrating sphere operating in reflectance mode. Polycrystalline powders were pulverized and diluted in mulls with $BaSO_4$ by a factor of 20, by mass, and pressed into sample pucks which were sealed inside the glovebox. The sample pucks were mounted at the rear of the integrating sphere for measurement. A sample puck filled with pure $BaSO_4$ was used as a blank. The obtained reflectance spectra were converted to absorbance using the Kubelka–Munk transformation.[21]

X-ray photoelectron spectroscopy (XPS) data were collected using a ThermoFisher Kα X-ray Photoelectron Spectrometer equipped with an Al Kα monochromated X-ray source. Polycrystalline samples of $KBaTiCl_6$ and $KBaVCl_6$, along with $TiCl_3$ and VCl_3 reagent standards, were affixed to copper tape in a N_2-filled glovebox and transferred to the instrument using a vacuum transfer module.

RESULTS AND DISCUSSION

Synthesis and Structure. The solids $A^IA^{II}B^{III}Cl_6$ (A^I = Na, K, Rb, Cs; A^{II} = Sr, Ba; B^{III} = Ti, V, Cr, Ir) and $Ba_{1.5}B^{III}Cl_6$ (B^{III} = V, Cr) were synthesized as polycrystalline powders via solid-state reactions in sealed fused-silica ampules. While compositions with Cr and Ir retained the violet and brown colors of the constituent $CrCl_3$ and $IrCl_3$ salts, respectively, compositions with Ti and V were lime green and orange in color, respectively, in contrast to the brown $TiCl_3$ and VCl_3 starting reagents. The colors of the solids correlate with ultraviolet–visible diffuse reflectance spectroscopy (UV–vis), which showed peaks in the visible region for $KBaVCl_6$ and $KBaCrCl_6$ corresponding to d–d transitions of the transition metals and strong absorption onsets at 2.6, 3.2, and 3.7 eV for $KBaTiCl_6$, $KBaVCl_6$, and $KBaCrCl_6$, respectively, which may correspond to their bandgaps (Figure S1). For most compositions, an excess of the diamagnetic ACl_2 starting reagent was required to avoid BCl_3 as a magnetic impurity in the product; the leftover ACl_2 in the product was quantified using Rietveld refinement of powder X-ray diffraction (PXRD)

https://doi.org/10.1021/acs.chemmater.4c01880
Chem. Mater. 2024, 36, 7610−7618

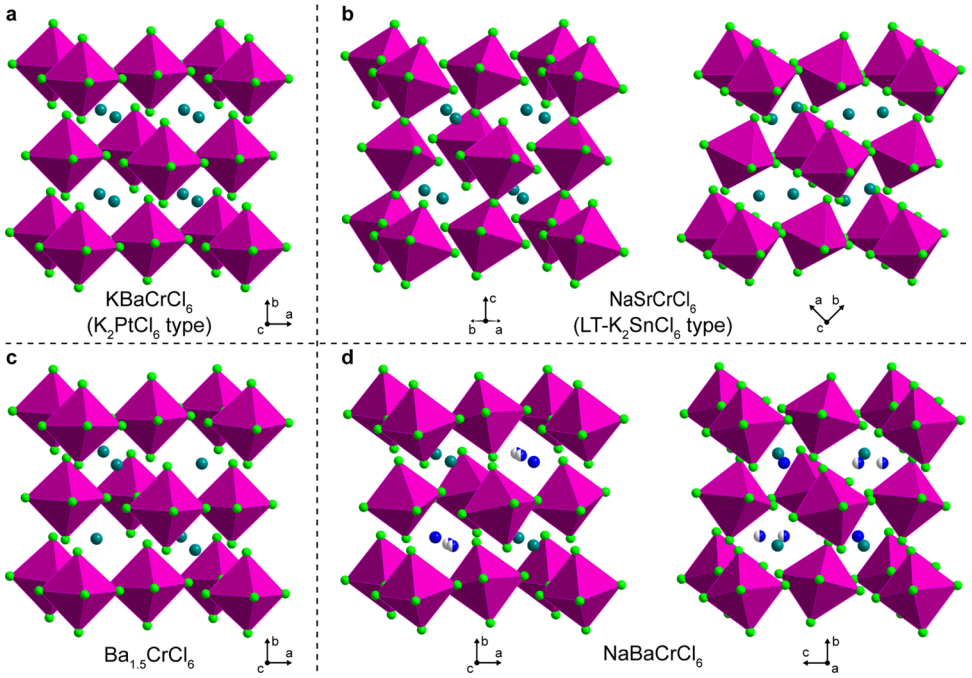

Figure 1. Single-crystal X-ray diffraction structures of $A^{I}A^{II}B^{III}Cl_6$ and $Ba_{1.5}B^{III}Cl_6$. (a) The K_2PtCl_6-type structure using $KBaCrCl_6$ as a representative example, where teal spheres represent mixed-occupancy K/Ba atoms. (b) The low-temperature (LT) K_2SnCl_6-type structure using $NaSrCrCl_6$ as a representative example, where teal spheres represent mixed-occupancy Na/Sr atoms. (c) The new $Ba_{1.5}CrCl_6$-type structure with ordered Ba vacancies, where teal spheres represent Ba atoms. (d) The new $NaBaCrCl_6$-type structure with ordered Na/Ba atoms, shown in two orientations, where blue and teal spheres represent Na and Ba atoms, respectively. The split occupancy of one of the Na sites is indicated by the half-filled spheres. Pink octahedra represent $Cr^{III}Cl_6$ and light green spheres represent Cl atoms.

data. The composition $CsBaTiCl_6$ additionally contained 28.7% by mass of the magnetic impurity $Cs_3Ti_2Cl_9$.

As is typical of first-row transition-metal halides, which often hydrate or oxidize upon exposure to water and oxygen, the compositions reported here were generally unstable to ambient conditions: $KBaTiCl_6$ and $KBaVCl_6$ nearly completely decomposed within minutes of exposure to ambient atmosphere, while $KBaCrCl_6$ decomposed more slowly, taking hours to fully decompose (Figures S2−S4). Additionally, given the instability of the 3+ oxidation state of Ti and the propensity for V to adopt multiple oxidation states, we confirmed the 3+ oxidation states of V and Ti in $KBaVCl_6$ and $KBaTiCl_6$, respectively, using X-ray photoelectron spectroscopy (Figure S5).

The compositions reported here crystallized in four distinct structure types, as determined using single-crystal X-ray diffraction (SCXRD; Tables S1−S24). While at least one composition in each of the four structure types was characterized using SCXRD, some compositions were unable to be characterized using SCXRD; Rietveld refinement of PXRD data was used in these cases to estimate the unit-cell volumes and radius ratios (see below; Table 1), though the radius ratios should be viewed as only approximations due to the low reliability of atomic positions from Rietveld refinement of laboratory PXRD data (Figures S6−S16 and Tables S25−S47). Compositions with the largest A-site cations (A^{I}/A^{II} = K/Ba, Rb/Ba, Cs/Ba) formed undistorted vacancy-ordered double perovskites with the K_2PtCl_6 structure type in the cubic space group $Fm\bar{3}m$ (no. 225; Figure 1a).[22] The two A-site cations were disordered, having 50% occupancy of each cation at the A site. Compositions with smaller A-site cations formed distorted vacancy-ordered double perovskites in one of two structure types: A^{I}/A^{II} = Na/Sr, K/Sr yielded perovskites with a low-temperature-K_2SnCl_6-type structure with disordered 50:50 occupancy of the cations at the A site in the monoclinic space group $P2_1/n$ (no. 14; Figure 1b),[23] while A^{I}/A^{II} = Na/Ba formed perovskites with a new subtype of distorted vacancy-ordered double perovskites with crystallographic ordering of the two A-site cations in the tetragonal space group $P4_2/n$ (no. 86; Figure 1d). We refer to the tetragonal structure here as the $NaBaCrCl_6$ type. Depending on the identity of the B-site cation, A^{I}/A^{II} = Rb/Sr formed perovskites with either the monoclinic low-temperature-K_2SnCl_6 structure type, as in $RbSrVCl_6$, or with the cubic K_2PtCl_6 structure type, as in $RbSrCrCl_6$ (Table 1). Finally, compositions with only Ba at the A site formed another new subtype of vacancy-ordered double perovskites with the formula $Ba_{1.5}MCl_6$ in the orthorhombic space group $I2_12_12_1$ (no. 24), having doubled lattice parameters with respect to those of the K_2PtCl_6-type structures (Figure 1c). For charge balance, 1:4 of the A sites are vacant in this structure; this yields the unit-cell doubling, which occurs from the crystallographic ordering of the A-site cations and vacancies with respect to one another. We refer to this structure here as the $Ba_{1.5}CrCl_6$ type.

Octahedral tilting in perovskites results from geometric mismatch between the size of the A-site cations and the metal−anion octahedra. In vacancy-ordered double perovskites, this can be quantified by the radius ratio

$$R = \frac{r_A}{D_{XX} - r_X} \tag{4}$$

where R is the radius ratio, r_A is the radius of the A-site cation, D_{XX} is the interoctahedral halide−halide distance, and r_X is the radius of the halide.[24,25] Empirically, it has been found that radius ratios of 0.89−1.00 result in cubic, K_2PtCl_6-type perovskites at room temperature (25 °C; RT), while values

https://doi.org/10.1021/acs.chemmater.4c01880
Chem. Mater. 2024, 36, 7610−7618

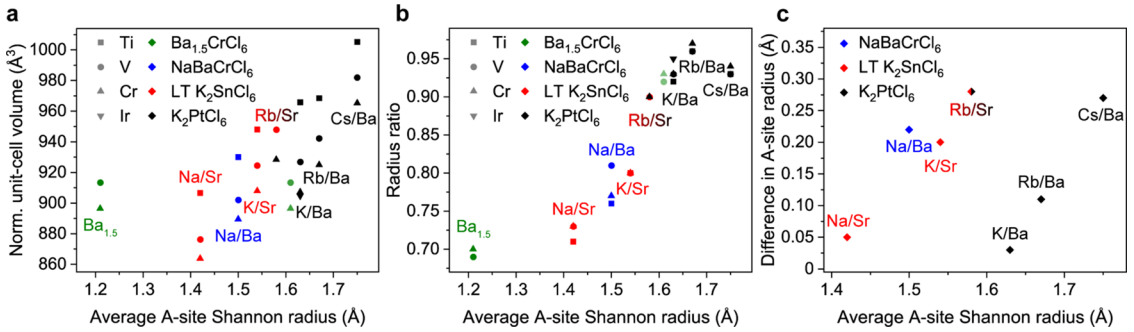

Figure 2. Dependence of crystallographic parameters on A-site Shannon radius in $A^IA^{II}B^{III}Cl_6$ and $Ba_{1.5}B^{III}Cl_6$. (a) The normalized unit-cell volume, (b) the radius ratio, and (c) the different in A-site radius between the two unique A-site cations as a function of the average Shannon radius of the A-site cations. The data points are grouped by B-site metal (shape) and by structure type (color). For $Ba_{1.5}CrCl_6$, the average A-site Shannon radius was calculated as 3:4 of the Shannon radius of Ba^{2+} for the opaque green data points and as the full Shannon radius of Ba^{2+} for the semitransparent green data points. The $Ba_{1.5}CrCl_6$ structure type is not shown in (c). The dual-color data point in (c) indicates that the structure type adopted by the compositions with Rb/Sr as the A-site cation combination depends on the identity of the B-site cation.

that are smaller than 0.89 yield perovskites with octahedral tilting to fill in the space left by A-site cations which are too small relative to the octahedra. Consistent with this prediction, the radius ratios of the K_2PtCl_6-type perovskites reported here range from 0.92 to 0.95, when using the average Shannon radius of the two A-site cations and the structural parameters derived from SCXRD, excluding $RbSrCrCl_6$ (Table 1).[26] Likewise, when considering the average of the Cl−Cl distances within 4 Å, the radius ratios range from 0.69 to 0.81 in the perovskites not in the K_2PtCl_6 structure type, excluding $RbSrVCl_6$; this yields octahedral tilting, described by the Glazer notations $a^+b^-b^-$ and $a^+a^+a^-$ for the low-temperature-K_2SnCl_6 and $NaBaCrCl_6$ structure types, respectively.[27] The radius ratio formalism furthermore explains why the K_2PtCl_6-type $RbSrCrCl_6$, which has a borderline radius ratio of 0.872, undergoes symmetry reduction upon replacement of Cr with V: the larger V^{3+} cation at the B site increases the interoctahedral Cl−Cl distance, which reduces the radius ratio to 0.867 and yields a lower-symmetry structure, suggesting that 0.87 is the lower-limit of radius ratio below which the K_2PtCl_6-type structure will not form in these perovskites. This change in radius ratio between $RbSrCrCl_6$ and $RbSrVCl_6$ is consistent with the reduction in radius ratio observed when replacing Cr with V in compositions with A^I/A^{II} = K/Ba, Rb/Ba, and Cs/Ba.

In contrast, the $Ba_{1.5}CrCl_6$ structure type is not readily described by radius ratios due to the ordered A-site vacancy. While using 3:4 of the Shannon radius of Ba^{2+} (the average radius including the A-site vacancy) yields a radius ratio of 0.70 for $Ba_{1.5}CrCl_6$, using the full Shannon radius of Ba^{2+} yields a value of 0.93, which suggests that the A-site vacancy destabilizes the K_2PtCl_6-type structure. While the SCXRD data for $Ba_{1.5}CrCl_6$ initially suggested a cubic structure, PXRD data revealed a subtle peak splitting consistent with a lower-symmetry structure (Figures S8 and S13); examination of precession images (Figure S17) and Pawley and Rietveld refinement of PXRD yielded the orthorhombic space-group assignment of $I2_12_12_1$ (no. 24). The drop in symmetry from cubic to orthorhombic suggests that the cubic structure is disrupted by subtle octahedral distortion and/or tilting that occurs to fill in the space left by the A-site vacancies, consistent with the radius ratio analysis which suggests that the structure is stable around the filled A sites but destabilized around the A-site vacancies.

The unit-cell volume of these vacancy-ordered double perovskites is directly dependent on the ionic radius of the B-site cation, increasing as expected from Cr to V to Ti for a given A-site composition (Figure 2a). However, the unit-cell volume of $KBaIrCl_6$ is smaller than that of $KBaB^{III}Cl_6$ (B^{III} = Cr, V, Ti), despite it having the largest Shannon radius; this may be a result of the enhanced covalency of metal halides as compared to the metal chalcogenides from which the Shannon radii are largely derived, a well-established shortcoming of the Shannon radii.[28] Similarly, the normalized unit-cell volume increases with the average A-site Shannon radius, with three exceptions. First, the normalized unit-cell volumes of $Ba_{1.5}VCl_6$ and $Ba_{1.5}CrCl_6$ are larger than those of $NaBaVCl_6$ and $NaBaCrCl_6$, respectively, despite having the smallest A-site radius when averaging over both occupied and unoccupied A sites. This inconsistency further emphasizes the unique nature of the $Ba_{1.5}CrCl_6$ structure type, where the coexistence of filled and vacant A sites prevents direct comparison with $A^IA^{II}B^{III}Cl_6$. Second, replacing Sr with the larger Ba in $KSrCrCl_6$ to form $KBaCrCl_6$ slightly reduces the unit-cell volume, which may be due to the change in structure type.[29] Third, the Rb/Sr A-site combination yields compositions with abnormally large unit-cell volumes; for instance, replacing Sr with Ba in $RbSrCrCl_6$ to yield $RbBaCrCl_6$ results in a unit-cell contraction, despite the increased average A-site Shannon radius. This may be due to the borderline radius ratio of compositions with Rb/Sr, which yields local octahedral tilting that expands the structure. This is evidenced by the SCXRD structure solution for $RbSrCrCl_6$, which reveals much larger thermal ellipsoids of the Cl atoms as compared to the other K_2PtCl_6-type structures, for example $KBaCrCl_6$, consistent with local octahedral tilting; indeed, dynamic octahedral tilting has been previously observed in VDPs.[30] We note that $KBaTiCl_6$, which has a relatively small radius ratio for the K_2PtCl_6 structure type, appears to have an unresolved crystallographic superstructure (Figure S17), which we speculate may be related to partially ordered octahedral tilting that stabilizes the structure.

We postulate that the A-site ordering in the $NaBaCrCl_6$-type structure, which is seldom observed in halide perovskites, is driven by size: A-site cations with similar ionic radii (Na/Sr and K/Sr) can occupy each other's crystallographic positions, while those with substantially different radii (Na/Ba and Ba/vacancy) cannot easily substitute for one another and therefore occupy distinct crystallographic sites (Figure 3c). While Rb/Sr

https://doi.org/10.1021/acs.chemmater.4c01880
Chem. Mater. 2024, 36, 7610−7618

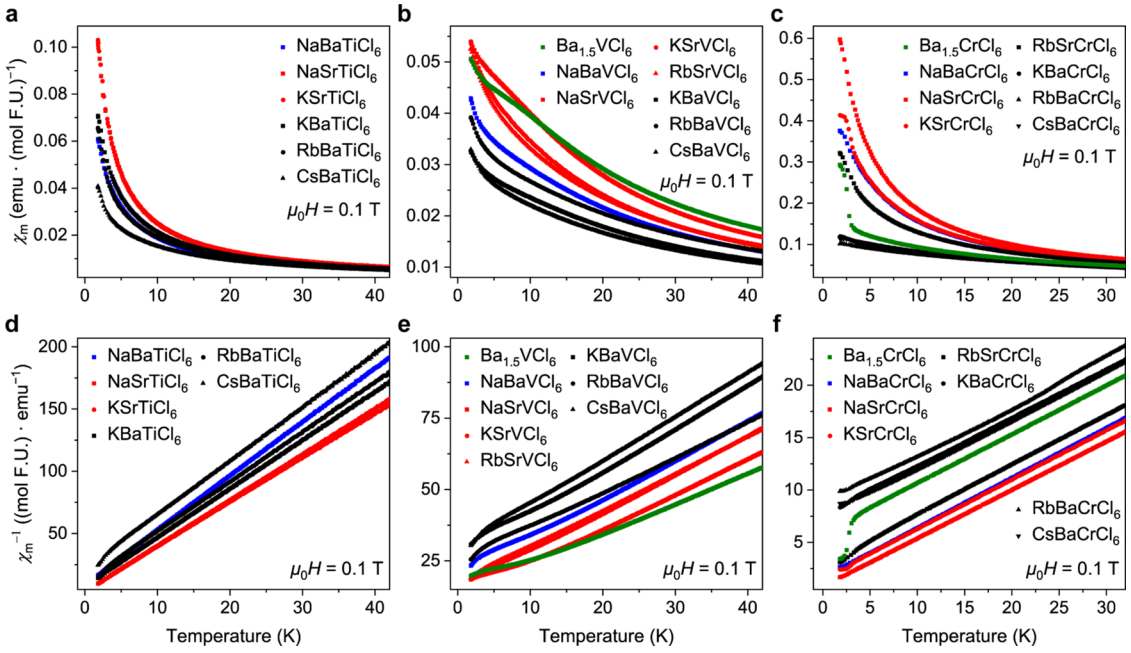

Figure 3. Temperature-dependent magnetic susceptibility (χ) from zero-field-cooled DC magnetization data using an applied field (μ_0H) of 0.1 T. Comparison of χ for: (a) $A^IA^{II}Ti^{III}Cl_6$; (b) $A^IA^{II}V^{III}Cl_6$ and $Ba_{1.5}V^{III}Cl_6$; and (c) $A^IA^{II}Cr^{III}Cl_6$ and $Ba_{1.5}Cr^{III}Cl_6$. Comparison of χ^{-1} for: (d) $A^IA^{II}Ti^{III}Cl_6$; (e) $A^IA^{II}V^{III}Cl_6$ and $Ba_{1.5}V^{III}Cl_6$; and (f) $A^IA^{II}Cr^{III}Cl_6$ and $Ba_{1.5}Cr^{III}Cl_6$. Within each plot, the data are grouped by structure type: data plotted in green, blue, red, and black correspond to the $Ba_{1.5}CrCl_6$, $NaBaCrCl_6$, LT-K_2SnCl_6, and K_2PtCl_6 structure types, respectively. A correction term, χ_0, was added to the data in (a, b), (d, e), as indicated in Table 2.

Table 2. Results of Curie–Weiss Fitting to Magnetic Susceptibility

structure type	composition	C (K emu · (mol F.U.)$^{-1}$)	Θ_{CW} (K)	μ_{eff} (μ_B)	spin-only moment (μ_B)	χ_0 (emu · (mol F.U.)$^{-1}$))
$Ba_{1.5}CrCl_6$	$Ba_{1.5}VCl_6$	0.88(2)	−7.6(2)	2.65(5)	2.83	+0.000408(8)
	$Ba_{1.5}CrCl_6$	2.03(2)	−7.83(8)	4.03(4)	3.87	0
$NaBaCrCl_6$	$NaBaTiCl_6$	0.232(4)	−2.74(9)	1.36(3)	1.73	+0.000396(7)
	$NaBaVCl_6$	0.808(10)	−25.4(3)	2.53(3)	2.83	+0.000782(11)
	$NaBaCrCl_6$	2.02(2)	+0.22(3)	4.02(4)	3.87	0
LT K_2SnCl_6	$NaSrTiCl_6$	0.274(6)	−1.46(8)	1.48(3)	1.73	+0.000623(13)
	$NaSrVCl_6$	0.778(9)	−6.30(10)	2.49(3)	2.83	+0.000733(9)
	$NaSrCrCl_6$	2.20(3)	−2.24(4)	4.19(6)	3.87	0
	$KSrTiCl_6$	0.280(6)	−0.99(9)	1.50(3)	1.73	+0.000326(7)
	$KSrVCl_6$	0.736(11)	−11.0(2)	2.41(4)	2.83	+0.00181(3)
	$KSrCrCl_6$	2.08(2)	−1.13(4)	4.08(3)	3.87	0
	$RbSrVCl_6$	0.81(2)	−18.3(4)	2.54(5)	2.83	+0.000489(12)
K_2PtCl_6	$RbSrCrCl_6$	2.01(3)	−1.00(4)	4.01(5)	3.87	0
	$KBaTiCl_6$	0.257(5)	−2.36(9)	1.43(3)	1.73	+0.000548(10)
	$KBaVCl_6$	0.729(7)	−29.7(3)	2.41(2)	2.83	+0.000702(8)
	$KBaCrCl_6$	2.03(2)	−10.97(11)	4.03(4)	3.87	0
	$RbBaTiCl_6$	0.251(5)	−3.18(10)	1.42(3)	1.73	+0.00104(2)
	$RbBaVCl_6$	0.814(12)	−21.6(3)	2.55(4)	2.83	+0.00129(2)
	$RbBaCrCl_6$	1.98(2)	−12.33(12)	3.98(4)	3.87	0
	$CsBaTiCl_6$[a]	0.225(3)	−3.55(14)	1.34(2)	1.73	+0.000613(9)
	$CsBaVCl_6$	0.672(8)	−23.3(3)	2.32(3)	2.83	+0.000934(12)
	$CsBaCrCl_6$	2.01(2)	−10.31(8)	4.01(3)	3.87	0

[a]Contained 28.7% by mass of a magnetic $Cs_3Ti_2Cl_9$ impurity.

and Cs/Ba also have substantially different ionic radii, the larger unit-cell volume of $RbSrVCl_6$ and $CsBaB^{III}Cl_6$ compared to $NaBaB^{III}Cl_6$ allows Rb/Sr and Cs/Ba to share a single crystallographic site in these structures. Combinations of Cs/Sr did not form the intended products, suggesting that there is an upper limit to the difference in A-site ionic radius that can be accommodated by these perovskites. Attempts to form $A^IA^{II}B^{III}Cl_6$ perovskites using either A^I = Li or A^{II} = Ca and attempts to form $Sr_{1.5}B^{III}Cl_6$ were unsuccessful under the current experimental conditions, which indicates that there is a lower limit to the ionic radius of the A-site cation that can be incorporated into these materials. Attempts to form $KBaM^{III}Cl_6$ (M = Fe, Mo, Ru, Rh, Au, Eu), $Ba_{1.5}TiCl_6$, and $RbSrTiCl_6$ were similarly unsuccessful, which may indicate an intrinsic instability of these compositions, though we continue

https://doi.org/10.1021/acs.chemmater.4c01880
Chem. Mater. 2024, 36, 7610−7618

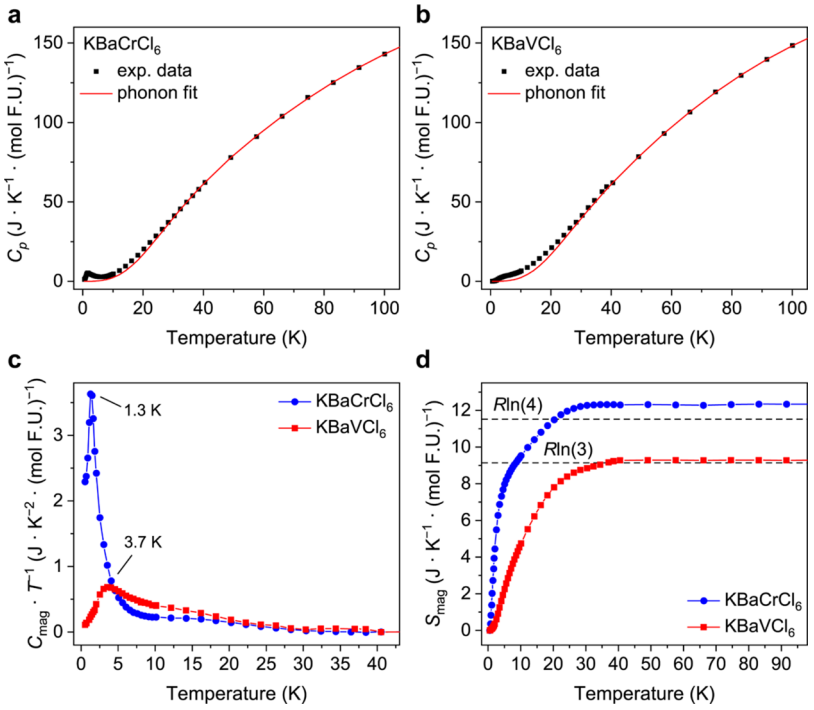

Figure 4. Heat-capacity measurements of $KBaCrCl_6$ and $KBaVCl_6$. Heat-capacity measurements and phonon fits using a two-component Debye model for (a) $KBaCrCl_6$ and (b) $KBaVCl_6$. (c) $C_{mag} \cdot T^{-1}$ versus T obtained by subtraction of the phonon fits. (d) Magnetic entropy (S_{mag}), with dashed lines showing the expected entropy for V^{3+} [$R\ln(3)$] and Cr^{3+} [$R\ln(4)$], where R is the gas constant.

to explore experimental conditions which may allow for their synthesis.

Magnetic Properties. To investigate the magnetism of $A^IA^{II}B^{III}Cl_6$ (A^I = Na, K, Rb, Cs; A^{II} = Sr, Ba; B^{III} = Ti, V, Cr) and $Ba_{1.5}B^{III}Cl_6$ (B^{III} = V, Cr), we first employed direct-current (DC) magnetization measurements from 1.8 to 300 K using an applied field of 0.1 T to extract temperature-dependent magnetic susceptibility (χ). These measurements revealed magnetic behavior dependent on both B-site-metal identity and structure type. The magnetic susceptibilities of the compositions containing Ti appeared paramagnetic, with no discernible deviations from Curie−Weiss behavior after a temperature-independent correction term (χ_0) was subtracted (Figure 3a,d and Table 2). Curie−Weiss fitting of the corrected inverse susceptibility revealed small, negative values of Curie−Weiss temperature (Θ_{CW}), consistent with paramagnetic behavior or very weak antiferromagnetic coupling (Table 2). In contrast, the magnetic susceptibilities of Cr-based compositions exhibited downturns in magnetic susceptibility below ∼3 K (Figure 3c,f), while V-based compositions showed a broad feature that appeared as a flattening of the susceptibility centered at ∼12 K (Figure 3b,e). In addition, the values of Θ_{CW} derived from Curie−Weiss fitting were negative and were larger in magnitude for the V-based compositions, after subtraction of a χ_0. The values of magnetic moment (μ_{eff}) extracted from Curie−Weiss fitting were consistent with the expected spin-only values for Ti^{3+}, V^{3+}, and Cr^{3+} (Table 2). Measurements of field-dependent magnetization revealed linear behavior at low fields with no saturation observed up to the highest measured field of 9 T (Figures S18−S25). Furthermore, no bifurcation was observed between zero-field-cooled and field-cooled susceptibilities for any composition (Figure S26). These results are consistent with antiferromagnetic interactions that are stronger in the V-based compositions than in the Cr-based compositions and negligible in the Ti-based compositions.

To rule out the possibility that VCl_3, which has a broad peak in susceptibility at ∼25 K, was present as impurity and responsible for the broad feature observed in the magnetic susceptibilities of the V-based compositions, we collected magnetic susceptibilities of pure VCl_3 and a sample of $KBaVCl_6$ mixed with 10 wt % VCl_3 (Figure S27). Instead of accentuating the broad feature in susceptibility at ∼12 K, the feature was suppressed in the sample spiked with VCl_3 due to the downturn in susceptibility for VCl_3, indicating that VCl_3 was not responsible for the feature.

In addition to the B-site identity, the crystal structure strongly influenced the magnetism in the Cr- and V-based compositions. The magnetic susceptibility at 1.8 K was lowest and the magnitude of the negative Θ_{CW} value largest for the V- and Cr-based compositions in the K_2PtCl_6 structure type, for example reaching values of −29.7(3) K and −10.97(11) K for $KBaVCl_6$ and $KBaCrCl_6$, respectively (Figure 3 and Table 2). This is consistent with the notion that the overlap between adjacent Cl p orbitals, and therefore the magnetic super-superexchange interactions, will be strongest when M−Cl···Cl−M is colinear, which is the case only in the K_2PtCl_6 structure type.[7] Indeed, the only exception to this trend of stronger apparent magnetic interactions in the K_2PtCl_6 structure type is $RbSrCrCl_6$, which likely has local octahedral tilting (see Synthesis and Structure section) that decreases the Cl···Cl p-orbital overlap. Both structures in the $Ba_{1.5}CrCl_6$ type are outliers, exhibiting a broad and exceptionally strong peak centered at ∼8 K in the magnetic susceptibility for $Ba_{1.5}VCl_6$ and a sharp upturn in susceptibility at ∼3 K for $Ba_{1.5}CrCl_6$. These anomalies indicate the possible presence of competing antiferromagnetic and ferromagnetic interactions and may be related to local octahedral ordering around the A-site vacancies

https://doi.org/10.1021/acs.chemmater.4c01880
Chem. Mater. 2024, 36, 7610−7618

at low temperatures, though further analysis will be required to examine these possibilities.

We further probed the magnetism of $KBaCrCl_6$ and $KBaVCl_6$ using heat-capacity measurements, where we extracted magnetic heat capacity (C_{mag}) by subtracting the phonon contribution using a two-component Debye model (Figure 4). This analysis revealed a sharp peak in $C_{mag} \cdot T^{-1}$ at 1.3 K for $KBaCrCl_6$, indicative of long-range magnetic ordering. In contrast, $KBaVCl_6$ showed a broad peak in $C_{mag} \cdot T^{-1}$ at 3.7 K that is suggestive of short-range or low-dimensional magnetic ordering, rather than long-range three-dimensional ordering. The shape and temperature of the peaks were minimally affected by applied magnetic fields for both compositions, consistent with relatively strong magnetic interactions. The magnetic entropy reached the expected values of $R\ln(2S + 1)$ for Heisenberg spin systems, where R is the gas constant and S is the magnetic spin, at temperatures of ~30 K and ~40 K for $KBaCrCl_6$ and $KBaVCl_6$, respectively.

Taken together, the magnetization and heat-capacity measurements indicate the presence of short-range antiferromagnetic ordering in $A^IA^{II}B^{III}Cl_6$ (B^{III} = V, Cr) with the K_2PtCl_6 structure type. As indicated by heat-capacity measurements, long-range magnetic ordering occurs at ~1.3 K for $KBaCrCl_6$, which is about an order of magnitude lower than its Θ_{CW} of −10.97(11) K, as extracted from magnetization measurements. $KBaVCl_6$ gives no indication of long-range magnetic ordering down to the lowest measured temperature of 0.5 K, nearly 2 orders of magnitude lower than its Θ_{CW} of −29.7(3) K. However, the entropy loss up to ~30 and ~40 K for $KBaCrCl_6$ and $KBaVCl_6$, respectively, suggests that both compositions exhibit short-range ordering up to temperatures which are more commensurate with their values of Θ_{CW}. Such behavior is precedented for this structure type, where the face-centered-cubic arrangement of the magnetic cations is geometrically frustrated for antiferromagnetically coupled spins and therefore prevents long-range ordering; indeed, similar magnetic behavior has been observed for the VDP K_2IrCl_6.[31]

Our magnetic characterization reveals a dependence of magnetism on both composition and structure. While the overlap of adjacent Cl p orbitals readily explains the structural dependence of magnetism in $A^IA^{II}B^{III}Cl_6$ and $Ba_{1.5}B^{III}Cl_6$, the compositional dependence is not as straightforward. The paramagnetic behavior of the compositions with Ti^{3+} is unsurprising, given the small magnetic moment of Ti^{3+} and the relatively large separation of the octahedra. However, the same logic applied to compositions with V^{3+} and Cr^{3+} would predict the strongest magnetic interactions in compositions with Cr^{3+}, with their larger magnetic moments and smaller interoctahedral distances, which directly conflicts with the experimental results. We speculate that competing antiferromagnetic and ferromagnetic interactions may be present in these materials, which would average out to yield values of Θ_{CW} which misrepresent the strength of the magnetic interactions. Further studies will be required to probe this hypothesis, such as low-temperature crystallography, single-crystal magnetic characterization, and neutron scattering.

CONCLUSIONS

Here, we add new members to the family of vacancy-ordered halide double perovskites by substituting in divalent A-site cations, which allows trivalent B-site cations to be incorporated. Using this strategy, we form 22 distinct compositions comprising three different magnetic cations and spanning four structure types, including two novel structure types with A-site ordering. This wealth of magnetic solids enables a study of structure−magnetism relationships, which reveals a strong relationship between octahedral tilting, B-site identity, and magnetic coupling strength. Further examination of the magnetism of these materials through, for example, neutron diffraction may offer insight into the possibility of competing antiferromagnetic and ferromagnetic coupling. The ability to tune the magnetic properties by simple substitution of A- and B-site cations may provide a platform for next-generation data storage and spintronics applications. Furthermore, we hope this A-site substitution strategy will spur continued study into compositions containing trivalent B-site cations and perhaps inspire more exotic substitutions to further expand the rich class of vacancy-ordered halide double perovskites.

ASSOCIATED CONTENT

Supporting Information

The Supporting Information is available free of charge at https://pubs.acs.org/doi/10.1021/acs.chemmater.4c01880.

Ultraviolet−visible diffuse reflectance spectra; powder X-ray diffraction stability studies; X-ray photoelectron spectra; refinement of powder X-ray diffraction data; precession images from single-crystal X-ray diffraction of $Ba_{1.5}CrCl_6$ and $KBaTiCl_6$; magnetic susceptibility and Curie−Weiss fits; and tabulated crystallographic information from single-crystal X-ray diffraction and powder X-ray diffraction refinement (PDF)

Accession Codes

CCDC 2332346−2332361 contain the supporting crystallographic data for this paper. These data can be obtained free of charge via www.ccdc.cam.ac.uk/data_request/cif, or by emailing data_request@ccdc.cam.ac.uk, or by contacting The Cambridge Crystallographic Data Centre, 12 Union Road, Cambridge CB2 1EZ, U.K.; fax: + 44 1223 336033.

AUTHOR INFORMATION

Corresponding Authors

Kurt P. Lindquist − *Department of Chemistry, Princeton University, Princeton, New Jersey 08544, United States;* orcid.org/0000-0002-2107-2455; Email: kplindqu@gmail.com

Robert J. Cava − *Department of Chemistry, Princeton University, Princeton, New Jersey 08544, United States;* orcid.org/0000-0002-3294-6867; Email: rcava@princeton.edu

Authors

Teresa Lee − *Department of Chemistry, Princeton University, Princeton, New Jersey 08544, United States;* orcid.org/0000-0002-5124-1301

Xianghan Xu − *Department of Chemistry, Princeton University, Princeton, New Jersey 08544, United States;* orcid.org/0000-0001-6854-300X

Complete contact information is available at: https://pubs.acs.org/10.1021/acs.chemmater.4c01880

Notes

The authors declare no competing financial interest.

https://doi.org/10.1021/acs.chemmater.4c01880
Chem. Mater. 2024, 36, 7610−7618

■ ACKNOWLEDGMENTS

The research was supported by the U.S. Department of Energy, Office of Science, National Quantum Information Science Research Centers, Co-design Center for Quantum Advantage (C2QA) under contract number DE-SC0012704 and by the same agency under the contract number DE-FG02-98ER45706. The authors acknowledge the use of the Imaging and Analysis Center (IAC) operated by the Princeton Materials Institute at Princeton University, which is supported in part by the Princeton Center for Complex Materials (PCCM), a National Science Foundation (NSF) Materials Research Science and Engineering Center (MRSEC; DMR-2011750).

■ REFERENCES

(1) Green, M. A.; Ho-Baillie, A.; Snaith, H. J. The emergence of perovskite solar cells. *Nat. Photonics* **2014**, *8* (7), 506−514.
(2) Lin, K.; Xing, J.; Quan, L. N.; de Arquer, F. P. G.; Gong, X.; Lu, J.; Xie, L.; Zhao, W.; Zhang, D.; Yan, C.; Li, W.; Liu, X.; Lu, Y.; Kirman, J.; Sargent, E. H.; Xiong, Q.; Wei, Z. Perovskite light-emitting diodes with external quantum efficiency exceeding 20%. *Nature* **2018**, *562* (7726), 245−248.
(3) Chen, Z.; Xue, J.; Wang, Z.; Lu, H. Magnetic hybrid transition metal halides. *Mater. Chem. Front.* **2023**, *8* (1), 210−227.
(4) Lu, Y.; Wang, Q.; He, R.; Zhou, F.; Yang, X.; Wang, D.; Cao, H.; He, W.; Pan, F.; Yang, Z.; Song, C. Highly Efficient Spin-Filtering Transport in Chiral Hybrid Copper Halides. *Angew. Chem., Int. Ed.* **2021**, *60* (44), 23578−23583.
(5) Zhu, T.; Lu, X. Z.; Aoyama, T.; Fujita, K.; Nambu, Y.; Saito, T.; Takatsu, H.; Kawasaki, T.; Terauchi, T.; Kurosawa, S.; Yamaji, A.; Li, H. B.; Tassel, C.; Ohgushi, K.; Rondinelli, J. M.; Kageyama, H. Thermal multiferroics in all-inorganic quasi-two-dimensional halide perovskites. *Nat. Mater.* **2024**, *23* (2), 182−188.
(6) Wolf, N. R.; Connor, B. A.; Slavney, A. H.; Karunadasa, H. I. Doubling the Stakes: The Promise of Halide Double Perovskites. *Angew. Chem., Int. Ed.* **2021**, *60* (30), 16264−16278.
(7) Whangbo, M.-H.; Koo, H.-J.; Dai, D. Spin exchange interactions and magnetic structures of extended magnetic solids with localized spins: theoretical descriptions on formal, quantitative and qualitative levels. *J. Solid State Chem.* **2003**, *176* (2), 417−481.
(8) Vargas, B.; Ramos, E.; Perez-Gutierrez, E.; Alonso, J. C.; Solis-Ibarra, D. A Direct Bandgap Copper−Antimony Halide Perovskite. *J. Am. Chem. Soc.* **2017**, *139* (27), 9116−9119.
(9) Lin, Y.-P.; Hu, S.; Xia, B.; Fan, K.-Q.; Gong, L.-K.; Kong, J.-T.; Huang, X.-Y.; Xiao, Z.; Du, K.-Z. Material Design and Optoelectronic Properties of Three-Dimensional Quadruple Perovskite Halides. *J. Phys. Chem. Lett.* **2019**, *10* (17), 5219−5225.
(10) Babel, D. Die Kristallstruktur des quaternären Fluorids $BaLiCrF_6$. *Z. Anorg. Allg. Chem.* **1974**, *406* (1), 23−37.
(11) Courbion, G.; Jacoboni, C.; De Pape, R. The dimorphism of $LiMnFeF_6$: A new kind of cationic order in the structural type Na_2SiF_6. *J. Solid State Chem.* **1982**, *45* (1), 127−134.
(12) Schaffers, K. I.; Keszler, D. A. Structure of $LiSrAlF_6$. *Acta Crystallogr., Sect. C: Cryst. Struct. Commun.* **1991**, *47* (1), 18−20.
(13) Hemon, A.; Courbion, G. Synthesis and crystal structures of β-$NaSrCr_6$ and $NaSrFeF_6$. Structural correlations with A_2MF_6 compounds. *Eur. J. Solid State Inorg. Chem.* **1992**, *29* (3), 519−531.
(14) Toby, B. H.; Von Dreele, R. B. GSAS-II: The Genesis of a Modern Open-Source All-Purpose Crystallography Software Package. *J. Appl. Crystallogr.* **2013**, *46*, 544−549.
(15) Rietveld, H. M. A Profile Refinement Method for Nuclear and Magnetic Structures. *J. Appl. Crystallogr.* **1969**, *2* (2), 65−71.
(16) Bruker. *SAINT and SADABS*; Bruker AXS Inc.: Madison, WI, 2016.
(17) Sheldrick, G. M. A Short History of SHELX. *Acta Crystallogr., Sect. A: Found. Crystallogr.* **2008**, *64* (1), 112−122.
(18) Sheldrick, G. M. *SHELXL-97, A Program for Crystal Structure Refinement*, Göttingen, 1997.
(19) Dolomanov, O. V.; Bourhis, L. J.; Gildea, R. J.; Howard, J. A. K.; Puschmann, H. OLEX2: A Complete Structure Solution, Refinement and Analysis Program. *J. Appl. Crystallogr.* **2009**, *42* (2), 339−341.
(20) Müller, P.; Herbst-Irmer, R.; Spek, A. L.; Schneider, T. R.; Sawaya, M. R. *Crystal Structure Refinement: A Crystallographer's Guide to SHELXL*; Oxford University Press: Oxford, 2006; p 232.
(21) Kubelka, P.; Munk, F. Z. Ein Beitrag zur Optik der Farbanstriche. *Z. Tech. Phys.* **1931**, *12*, 593−601.
(22) Ewing, P. J.; Pauling, L. The Crystal Structure of Potassium Chloroplatinate. *Z. Kristallogr. - Cryst. Mater.* **1928**, *68* (1−6), 223−230.
(23) Boysen, H.; Hewat, A. W. A neutron powder investigation of the structural changes in K_2SnCl_6. *Acta Crystallogr., Sect. B: Struct. Crystallogr. Cryst. Chem.* **1978**, *34* (5), 1412−1418.
(24) Brown, I. D. The Crystal Structure of K_2TeBr_6. *Can. J. Chem.* **1964**, *42* (12), 2758−2767.
(25) Maughan, A. E.; Ganose, A. M.; Scanlon, D. O.; Neilson, J. R. Perspectives and Design Principles of Vacancy-Ordered Double Perovskite Halide Semiconductors. *Chem. Mater.* **2019**, *31* (4), 1184−1195.
(26) Shannon, R. D. Revised Effective Ionic Radii and Systematic Studies of Interatomic Distances in Halides and Chalcogenides. *Acta Crystallogr., Sect. A* **1976**, *32* (5), 751−767.
(27) Woodward, P. M. Octahedral Tilting in Perovskites. I. Geometrical Considerations. *Acta Crystallogr., Sect. B: Struct. Sci.* **1997**, *53* (1), 32−43.
(28) Travis, W.; Glover, E. N. K.; Bronstein, H.; Scanlon, D. O.; Palgrave, R. G. On the application of the tolerance factor to inorganic and hybrid halide perovskites: a revised system. *Chem. Sci.* **2016**, *7* (7), 4548−4556.
(29) Adams, D. J.; Churakov, S. V. Classification of perovskite structural types with dynamical octahedral tilting. *IUCrJ* **2023**, *10* (3), 309−320.
(30) Maughan, A. E.; Ganose, A. M.; Almaker, M. A.; Scanlon, D. O.; Neilson, J. R. Tolerance Factor and Cooperative Tilting Effects in Vacancy-Ordered Double Perovskite Halides. *Chem. Mater.* **2018**, *30* (11), 3909−3919.
(31) Ramirez, A. P. Strongly Geometrically Frustrated Magnets. *Annu. Rev. Mater. Sci.* **1994**, *24* (1), 453−480.

https://doi.org/10.1021/acs.chemmater.4c01880
Chem. Mater. 2024, 36, 7610−7618